Article

Hydrothermal Synthesis of ZnO–doped Ceria Nanorods: Effect of ZnO Content on the Redox Properties and the CO Oxidation Performance

Sofia Stefa [1], Maria Lykaki [1], Vasillios Binas [2], Pavlos K. Pandis [3], Vassilis N. Stathopoulos [3,*] and Michalis Konsolakis [1,*]

[1] Industrial, Energy and Environmental Systems Lab (IEESL), School of Production Engineering and Management, Technical University of Crete, GR-73100 Chania, Crete, Greece; sstefa@isc.tuc.gr (S.S.); mlykaki@isc.tuc.gr (M.L.)

[2] Institute of Electronic Structure and Laser, Foundation for Research and Technology-Hellas (FORTH–IESL), P.O. Box 1527, Vasilika Vouton, GR-71110 Heraklion, Greece; binasbill@iesl.forth.gr

[3] Laboratory of Chemistry and Materials Technology, General (Core) Department, National and Kapodistrian University of Athens, GR-34400 Psachna Campus, Evia, Greece; ppandis@teiste.gr

* Correspondence: vasta@uoa.gr (V.N.S.); mkonsol@pem.tuc.gr (M.K.); Tel.: +30-22280-99688 (V.N.S.); +30-28210-37682 (M.K.)

check for updates

Abstract: The rational design of highly efficient, noble metal-free metal oxides is one of the main research priorities in the area of catalysis. To this end, the fine tuning of ceria-based mixed oxides by means of aliovalent metal doping has currently received particular attention due to the peculiar metal-ceria synergistic interactions. Herein, we report on the synthesis, characterization and catalytic evaluation of ZnO–doped ceria nanorods (NR). In particular, a series of bare CeO_2 and ZnO oxides along with CeO_2/ZnO mixed oxides of different Zn/Ce atomic ratios (0.2, 0.4, 0.6) were prepared by the hydrothermal method. All prepared samples were characterized by X-ray diffraction (XRD), N_2 physisorption, temperature-programmed reduction (TPR), scanning electron microscopy with energy dispersive X-ray spectroscopy (SEM-EDS) and transmission electron microscopy (TEM). The CO oxidation reaction was employed as a probe reaction to gain insight into structure-property relationships. The results clearly showed the superiority of mixed oxides as compared to bare ones, which could be ascribed to a synergistic ZnO–CeO_2 interaction towards an improved reducibility and oxygen mobility. A close correlation between the catalytic activity and oxygen storage capacity (OSC) was disclosed. Comparison with relevant literature studies verifies the role of OSC as a key activity descriptor for reactions following a redox-type mechanism.

Keywords: CeO_2/ZnO mixed oxides; zinc oxide; ceria nanorods; oxygen storage capacity; CO oxidation

1. Introduction

Cerium oxide or ceria (CeO_2) is considered one of the most promising metal oxides for numerous catalytic applications, such as catalytic oxidation of CO [1–3], NO reduction [4–6], water–gas shift reaction [7–10], reforming reactions [11,12] and soot combustion [13–15]. In particular, CeO_2 has attracted extensive interest due to its abundant oxygen vacancies, interchangeability between Ce^{3+} and Ce^{4+} oxidation states and high oxygen storage capacity (OSC) [16–18]. During the past few decades, nanotechnology has made remarkable progress toward the development of ceria nanocomposites with distinct physical and chemical properties, greatly expanding their potential applications in energy and environmental catalysis [19,20]. In this perspective, we recently showed that among ceria

nanocomposites of different shape, ceria nanorods possess enhanced reducibility that is linked to their high population in intrinsic defects and oxygen vacancies. The latter is considered responsible for their superior CO oxidation performance [21].

More importantly, ceria-based mixed oxides have recently gained increasing attention in the fields of materials science and heterogeneous catalysis, due to their unique surface, structural and electronic properties, which are completely different to those of parent counterparts. The combination of various transition metals with CeO_2 nanoparticles leads to enhanced surface and redox properties due to the "synergistic" interactions between the oxide phases. Accordingly, various CeO_2–based transition metals (M/CeO_2, M = Mn, Fe, Co, Ni, Cu) have been widely employed in heterogeneous catalysis [22,23].

Among the different transition metal oxides, zinc oxide (ZnO) is a wide and direct band gap semiconductor, which has been used in many fields, due to its low cost and environmental sustainability [24–26]. Zinc is not a critical raw material, thus no direct impact on the environmental resources is considered. Moreover, it is abundant in the steel industry as one of the main recovered products in the metal scrap recycling process [27]. In view of this fact, the potential of a low-cost metal, able to further enhance the catalytic performance of CeO_2, is of particular importance both from an environmental and economic point of view.

Although CeO_2–ZnO composites have been extensively used in photocatalysis [28–32], only a few studies have been devoted to their catalytic applications. Xie et al. [33] reported on the enhanced CO oxidation activity of CeO_2–ZnO composites, which is ascribed to the synergistic interaction between ZnO hollow microspheres and commercial CeO_2 powders. In a similar manner, the synergistic interaction between ZnO and CeO_2 is considered responsible for the enhanced CO oxidation performance of three-dimensional ordered macroporous CeO_2–ZnO [34].

In light of the above aspects, the present work aims for a first time at investigating the impact of ZnO as modifier for ceria nanorods (NR), in an attempt to further adjusting their surface/redox properties. To this end, a series of pure CeO_2 and ZnO along with CeO_2/ZnO mixed oxides of different Zn:Ce atomic ratios (0.2, 0.4, 0.6) were prepared by the hydrothermal method. The as-prepared materials were thoroughly characterized by X-ray diffraction (XRD), N_2 adsorption at -196 °C (Brunauer–Emmett–Teller (BET) method), scanning electron microscopy-energy dispersive X-ray spectroscopy (SEM–EDS), transmission electron microscopy (TEM) and H_2 temperature-programmed reduction (H_2–TPR). The oxidation of CO was used as a probe reaction to disclose structure-activity relationships.

2. Materials and Methods

2.1. Materials Synthesis

All of the chemicals used in this work were of analytical reagent grade. $Ce(NO_3)_3 \cdot 6H_2O$ (purity ≥99.0%, Fluka, Bucharest, Romania), $Zn(CH_3COO)_2 \cdot 2H_2O$ (purity ≥99%, Sigma-Aldrich, St. Louis, MO, USA) were used as precursors for the preparation of ceria-zinc materials. HO_2CCO_2H (purity ≥99%, Sigma-Aldrich, St. Louis, MO, USA), NaOH (purity ≥98%, Honeywell Fluka, Seelze, Germany) and absolute ethanol (purity 99.8%, ACROS Organics, Geel, Belgium) were also employed during the synthesis procedure.

Bare ceria nanorods were initially prepared by the hydrothermal method, as described in detail in our previous work [21]. CeO_2/ZnO mixed oxides of different Zn:Ce ratios (0.2, 0.4, 0.6) were prepared by a modified hydrothermal method. In particular, 0.38 g HO_2CCO_2H, 0.64 g $Zn(CH_3COO)_2 \cdot 2H_2O$ and a certain quantity of CeO_2 nanorods (2.42, 1.21, 0.81 g for Zn/Ce = 0.2, 0.4 and 0.6, respectively), were dispersed in 40 mL of double deionized water under stirring for 20 min. Then, the suspension obtained was transferred to a plastic bottle and aged at 70 °C for 1 h. The precipitate was recovered by centrifugation, washed with double deionized water and ethanol, dried at room temperature overnight, and calcined at 500 °C for 2 h under air flow (heating ramp 5 °C/min). For comparison purposes, a pure

zinc oxide sample was also prepared by the same method. The as-prepared materials are denoted as CeO_2/ZnO–x, where x refers to Zn:Ce atomic ratio.

For comparison purposes, a mechanical mixture (CeO_2+ZnO–0.4) was synthesized in agate by hand, by physically mixing ceria nanorods and ZnO, with the same composition as the CeO_2/ZnO–0.4 sample.

2.2. Materials Characterization

The textural characteristics of the investigated samples were assessed by N_2 adsorption-desorption isotherms at −196 °C (Nova 2200e Quantachrome flow apparatus, Boynton Beach, FL, USA). The structural properties were determined by X-ray diffraction (XRD) in a Rigaku diffractometer (model RINT 2000, Tokyo, Japan). Morphological/surface analysis was performed by scanning electron microscopy (SEM, JEOL JSM-6390LV, JEOL Ltd., Akishima, Tokyo, Japan) operating at 20 keV, equipped with an energy dispersive X-ray spectrometry (EDS) system and transmission electron microscopy (TEM) on a JEM-2100 instrument (JEOL, Tokyo, Japan). Redox properties were determined by means of H_2 temperature-programmed reduction (H_2–TPR). More details about the aforementioned characterization studies and the corresponding apparatus can be found elsewhere [2,35].

2.3. Catalytic Evaluation Studies

Catalytic experiments were carried out in a fixed-bed reactor (12.95 mm i.d.) loaded with 100 mg of catalyst. Feed composition was 0.2 vol.% of CO and 1 vol.% O_2 balanced with He. The total feed stream was 80 cm^3 min^{-1}, corresponding to a gas hourly space velocity (GHSV) of 40,000 h^{-1}.

All samples were pretreated with 10 °C min^{-1} up to 490 °C (30 min) under 20 vol.% O_2 in He. Then, the temperature was leveled off to 25 °C, followed by He purging to remove any physisorbed species. Catalytic activity measurements were carried out up to 500 °C. Both reactants and products were analyzed by gas chromatography equipped with thermal conductivity detectors (TCD) and two capillary columns (Molecular Sieve 5X and PoraPlot Q).

CO conversion (X_{CO}) was calculated according to the equation:

$$X_{CO}(\%) = \frac{[CO]_{in} - [CO]_{out}}{[CO]_{in}} \times 100 \tag{1}$$

where $[CO]_{in}$ and $[CO]_{out}$ are the CO concentrations in the inlet and outlet gas streams, respectively.

Specific reaction rates of CO consumption, in terms of the catalyst's mass (mol g^{-1} s^{-1}) or surface area (mol m^{-2} s^{-1}) were estimated under differential reaction conditions (W/F = 0.075 g s cm^{-3}, X_{CO} < 15%, T = 200 °C):

$$r\left(\frac{mol}{g \cdot s}\right) = \frac{X_{CO} \times [CO]_{in} \times F\left(\frac{cm^3}{min}\right)}{100 \times 60\left(\frac{s}{min}\right) \times V_m\left(\frac{cm^3}{mol}\right) \times m_{cat}(g)} \tag{2}$$

$$r\left(\frac{mol}{m^2 \cdot s}\right) = \frac{X_{CO} \times [CO]_{in} \times F\left(\frac{cm^3}{min}\right)}{100 \times 60\left(\frac{s}{min}\right) \times V_m\left(\frac{cm^3}{mol}\right) \times m_{cat}(g) \times S_{BET}\left(\frac{m^2}{g}\right)} \tag{3}$$

where V_m and F are gas molar volume and total flow rate, respectively, at 298 K and 1 bar, m_{cat} is the mass of catalyst and S_{BET} is the surface area.

3. Results and Discussion

3.1. Textural and Structural Characterization

The determination of the textural properties (surface area, pore volume, pore size) of CeO_2/ZnO samples was carried out by means of nitrogen adsorption-desorption (BET) analysis.

The results obtained are summarized in Table 1. The lowest value in BET surface area is demonstrated by ZnO (7.05 m^2/g). CeO$_2$ nanorods exhibit the highest surface area (79.31 m^2/g) followed by CeO$_2$/ZnO–0.2 (76.22 m^2/g), CeO$_2$/ZnO–0.4 (62.21 m^2/g), CeO$_2$/ZnO–0.6 (56.12 m^2/g) and ZnO (7.05 m^2/g). In general, ZnO addition progressively decreases the BET surface area. This is also in agreement with the gradual increase of pore size with the increase of ZnO content, as discussed below.

Table 1. Textural characteristics of bare CeO$_2$, ZnO and the CeO$_2$/ZnO samples.

Sample	BET Analysis		
	Surface Area (m^2/g)	Pore Volume (cm^3/g)	Average Pore Size (nm)
CeO$_2$	79.31 ± 0.15	0.48	24.2
CeO$_2$/ZnO–0.2	76.22 ± 0.12	0.67	34.4
CeO$_2$/ZnO–0.4	62.21 ± 0.11	0.65	40.6
CeO$_2$/ZnO–0.6	56.12 ± 0.09	0.91	55.9
ZnO	7.05 ± 0.01	0.06	23.0

The adsorption-desorption isotherms and the Barrett–Joyner–Halenda (BJH) desorption pore size distribution (PSD) of as-prepared samples are shown in Figure 1a,b, respectively. The pore size distribution in all samples is well within the mesopores region, which is further corroborated by the existence of type IV isotherms (Figure 1a). As presented in Table 1 and Figure 1b, the addition of ZnO leads to an increase in pore volume and average pore size, with the CeO$_2$/ZnO–0.6 sample exhibiting the highest pore size (55.9 nm) followed by CeO$_2$/ZnO–0.4 (40.6 nm), CeO$_2$/ZnO–0.2 (34.4 nm), CeO$_2$ (24.2 nm) and ZnO (23.0 nm).
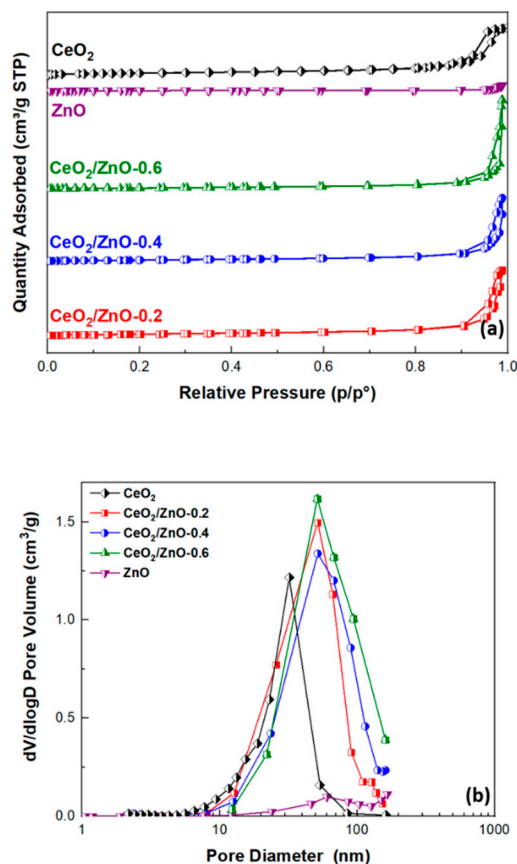

Figure 1. (**a**) N$_2$ adsorption-desorption isotherms and (**b**) pore size distribution of bare CeO$_2$, ZnO and the CeO$_2$/ZnO samples.

Figure 2 depicts the XRD patterns of CeO_2, ZnO and CeO_2/ZnO (Zn:Ce = 0.2, 0.4, 0.6) mixed oxide phases. The main diffraction peaks for bare ceria at $2\theta = 28.5°$, 33.1°, 47.5° and 56.3° correspond to (111), (200), (220) and (311) planes, respectively. The diffraction peaks are attributed to ceria face-centered cubic fluorite structure (Fm3m symmetry, no. 225) (JCPDS card: 01-081-0792). Similarly, the XRD patterns of pure ZnO exhibit the typical hexagonal wurtzite structures (P63mc symmetry, no. 186) (JCPDS card: 01-079-0208). The strong peaks at $2\theta = 31.7°$, 34.4° and 36.2° can be attributed to (100), (002), (101) lattice planes, respectively. For the CeO_2/ZnO samples, reflection planes perfectly matched to both indexed CeO_2 cubic and ZnO hexagonal structures. The XRD patterns indicate the formation of mixed oxides with finely dispersed phases of parent oxides. When ZnO content is increased, the intensity of ZnO reflections at (100), (002) and (101) is also increased, while the XRD profile of CeO_2 remains unaffected. The sharp diffraction peaks in the XRD patterns indicate that the synthesized catalysts are well crystallized. By applying the Scherrer equation, the average crystallite size of the as-prepared samples was calculated and the results are presented in Table 2. The lattice parameters are also included in Table 2. Bare CeO_2 exhibits a crystallite size of 13.0 nm, while pure ZnO exhibits a much larger crystallite size (34.5 nm). For the CeO_2/ZnO samples, ceria crystallite size displays a small decrease with the addition of ZnO, while the crystallite size of ZnO is increased. In addition, the lattice parameters of mixed oxides remain practically unaffected, as compared to the pure oxides, revealing well-dispersed phases of the different constituent oxides.
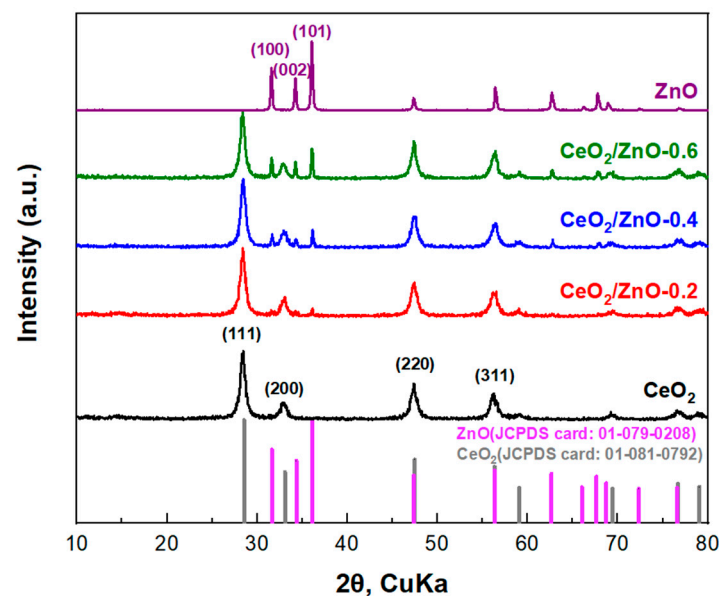

Figure 2. XRD patterns of CeO_2, ZnO and the CeO_2/ZnO samples.

Table 2. Structural characteristics of CeO_2, ZnO and the CeO_2/ZnO samples.

Samples	XRD Analysis			
	Phase Detected	Average Crystallite Size, D_{XRD} (nm)		Lattice Parameters (nm)
		CeO_2	ZnO	
CeO_2	Cerium (IV) oxide	12.99 ± 0.01	-	a = b = c = 0.5430 ± 0.0001
CeO_2/ZnO–0.2	Cerium (IV) oxide Zincite	12.14 ± 0.01	44.41 ± 0.05	a = b = c = 0.5439 ± 0.0001 a = b = 0.3180 ± 0.0001; c = 0.5232 ± 0.0001
CeO_2/ZnO–0.4	Cerium (IV) oxide Zincite	11.92 ± 0.01	44.65 ± 0.05	a = b = c = 0.5430 ± 0.0001 a = b = 0.3262 ± 0.0001; c = 0.5225 ± 0.0001
CeO_2/ZnO–0.6	Cerium (IV) oxide Zincite	11.56 ± 0.01	39.32 ± 0.05	a = b = c = 0.5439 ± 0.0001 a = b = 0.3267 ± 0.0001; c = 0.523 ± 0.0001
ZnO	Zincite	-	34.50 ± 0.05	a = b = 0.3272 ± 0.0001; c = 0.5233 ± 0.0001

3.2. Morphological Characterization (TEM, SEM–EDS)

The morphological features of CeO_2, ZnO and CeO_2/ZnO mixed oxides were characterized by transmission electron microscopy analysis (TEM). Pure ZnO (Figure 3a) displays an irregular shape (50–100 nm), while bare CeO_2 (Figure 3b) exhibits a distinct rod-like morphology (50–200 nm in length). In Figure 3c–e, the CeO_2/ZnO mixed oxides are presented. It is evident that the mixed oxides exhibit the rod-like morphology of CeO_2 nanorods, while separated ZnO particles of irregular morphology are also detected. These findings are in accordance with XRD results, implying the formation of distinct oxide phases.
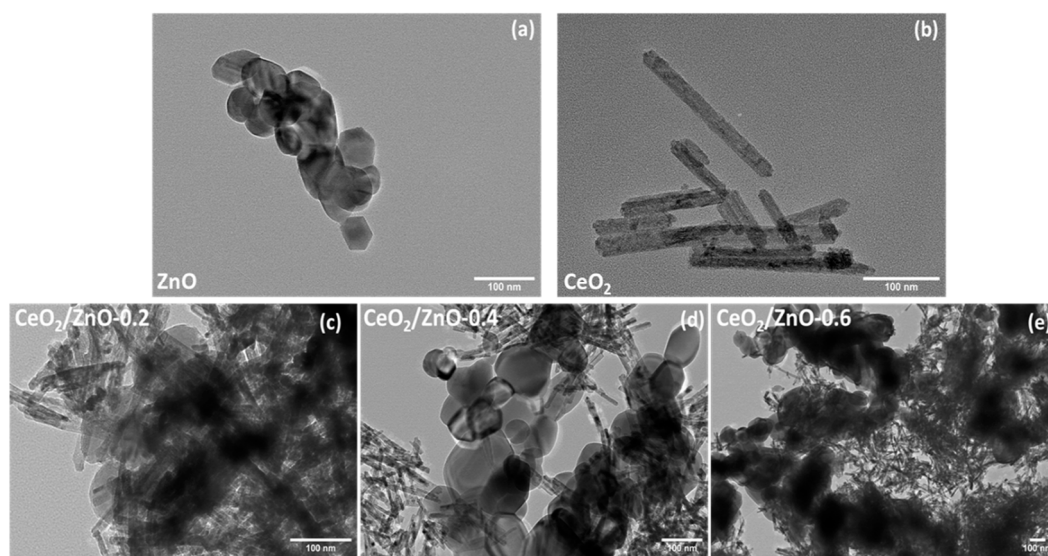

Figure 3. TEM images of (**a**) ZnO, (**b**) CeO_2, (**c**) CeO_2/ZnO–0.2, (**d**) CeO_2/ZnO–0.4 and (**e**) CeO_2/ZnO–0.6.

Elemental analysis was indicatively carried out by scanning electron microscopy analysis along with energy dispersive X-ray spectrometry (SEM–EDS) over the CeO_2/ZnO–0.2 sample. The SEM image along with the corresponding elemental analysis is shown in Figure 4. SEM–EDS analysis implies a Zn:Ce atomic ratio of ca. 0.19, being in good agreement with the nominal Zn/Ce ratio. The latter implies a uniform distribution of CeO_2 and ZnO phases on the entire material.
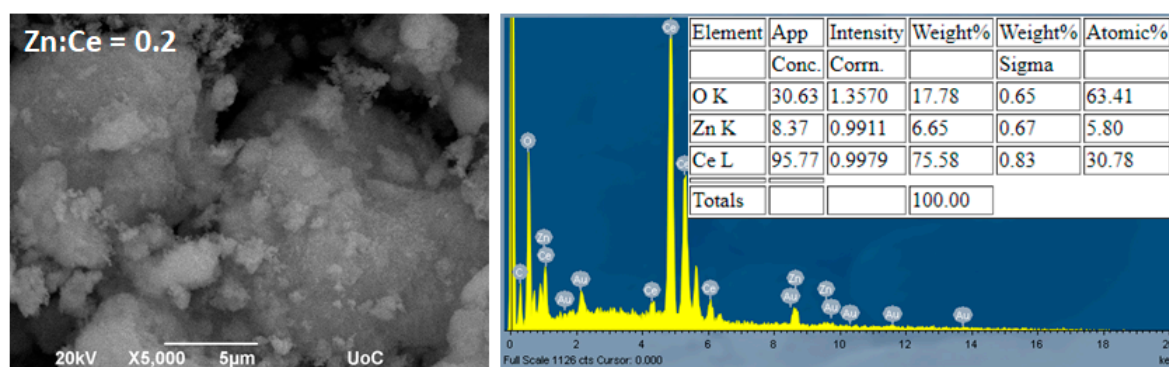

Figure 4. SEM–EDS analysis of the CeO_2/ZnO–0.2 sample.

3.3. Redox Properties (H_2–TPR)

By means of H_2–TPR experiments, the quality and quantity of the active oxygen sites of the catalysts can be determined. Such information is important for reactions following a redox-type mechanism, such as CO oxidation. Figure 5 shows the reduction profiles of bare and mixed oxides in the temperature range of 100–800 °C. The CeO_2 sample shows a peak at 500–700 °C (peak C),

which is ascribed to the loosely bound surface species, contrary to bulk oxygen, which is reduced at temperatures higher than 700 °C [1,36–38]. For the pure ZnO sample, two broad peaks are found located at 150–300 °C (peak A) and 410–530 °C (peak B) regions, which can be attributed to the reduction of the hydroxyl species related to ZnO and the surface oxygen reduction from ZnO, respectively [39]. Additionally, in the pristine ZnO, the Zn^{2+} reduction to Zn^0 has been reported at 465 °C [40]. The TPR profiles of CeO_2/ZnO samples consist of the distinct peaks of both CeO_2 and ZnO phases. It is worth noticing that ZnO addition to CeO_2 does not lead to a shift of TPR peaks, as recently found for CeO_2/TiO_2 [35] and Fe_2O_3/CeO_2 [2] mixed oxides. This implies the structurally independent nature of ZnO and CeO_2 in the mixed oxides. The latter is in agreement with XRD and TEM results showing distinct ZnO nanoparticles in the vicinity of CeO_2 nanorods without incorporation of Zn in the nanostructure of CeO_2 nanorods.
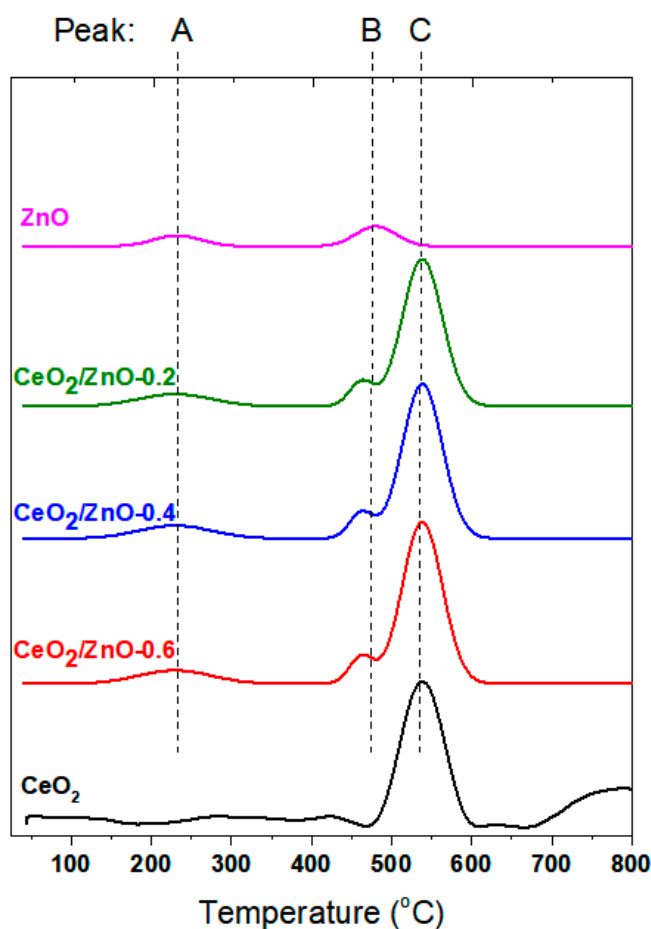

Figure 5. H_2-TPR profiles of CeO_2 and the CeO_2/ZnO samples.

To gain greater insight into the influence of ZnO on the reducibility of CeO_2/ZnO oxides, the H_2 uptake in the temperature range of 50–700 °C was estimated by the quantification of the TPR peaks (Table 3). Interestingly, ZnO addition results in an increase of H_2 uptake in the CeO_2/ZnO samples, implying a facilitation of surface oxygen species detachment. It is also of worth noticing the increase of H_2 uptake related to ceria reduction (peak C), despite the progressive decrease of ceria content. The latter denotes the facile reduction of ceria capping oxygen upon the increase of ZnO content. In particular, all mixed oxides exhibit a total H_2 consumption of ca. 1.0 mmol H_2/g, as compared to 0.59 and 0.31 mmol H_2/g of bare CeO_2 and ZnO, respectively. In terms of oxygen storage capacity (OSC), the following trend is obtained: CeO_2/ZnO–0.6 (0.52 mmol O_2/g) > CeO_2/ZnO–0.4 (0.50 mmol O_2/g) > CeO_2/ZnO–0.2 (0.48 mmol O_2/g) > CeO_2 (0.29 mmol O_2/g) > ZnO (0.15 mmol O_2/g). This order coincides relatively well with the catalytic activity (see below), revealing the key role of reducibility.

The abundance of reducible oxygen species is expected to affect the oxygen mobility and in turn the CO oxidation process, as will be further discussed below.

Table 3. Redox features of CeO_2 and CeO_2/ZnO samples.

Sample	H$_2$ Uptake (mmol H$_2$/g) and OSC (mmol O$_2$/g)				
	Peak A	Peak B	Peak C	H$_2$ uptake	OSC
CeO_2	-	-	0.59	0.59	0.29
CeO_2/ZnO–0.2	0.15	0.21	0.61	0.97	0.48
CeO_2/ZnO–0.4	0.15	0.23	0.63	1.01	0.50
CeO_2/ZnO–0.6	0.16	0.25	0.63	1.04	0.52
ZnO	0.14	0.17	-	0.31	0.15

3.4. Catalytic Evaluation Studies

In Figure 6, the conversion profiles of CO over temperature for bare ZnO, CeO_2 and CeO_2/ZnO mixed oxides are shown. It is evident that all mixed oxides demonstrate superior performance as compared to bare ones. A similar performance was obtained between mixed oxides, with the CeO_2/ZnO–0.4 being slightly better. To gain insight into the role of preparation method and the synergistic interaction between the different counterparts, the catalytic performance of a mechanical mixture (CeO_2+ZnO–0.4) of exactly the same composition to the optimum sample (CeO_2/ZnO–0.4) was explored in parallel. The bare ceria nanorods (CeO_2) exhibit a catalytic profile shifted by ca. 30 °C to higher temperature than the optimum CeO_2/ZnO–0.4 sample. ZnO is much less active with a profile located ca. 170 degrees higher. More importantly, the conversion profile of the mechanical mixture CeO_2+ZnO–0.4 is shifted by ca. 100 °C to higher temperatures as compared to that of CeO_2/ZnO–0.4, revealing the beneficial interaction between CeO_2 and ZnO, which is induced by the preparation method (see experimental Section 2.1).
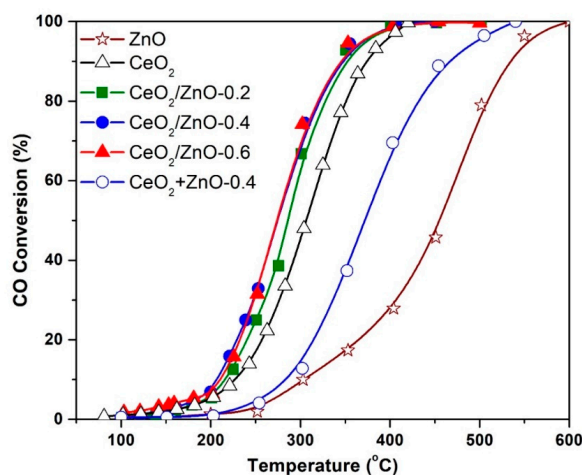

Figure 6. CO conversion profiles of CeO_2, ZnO and CeO_2/ZnO samples.

To obtain a better understanding in relation to the intrinsic activity of investigated samples, the specific activity, both in terms of catalyst mass (μmol g^{-1} s^{-1}) and surface area (μmol m^{-2} s^{-1}), was also estimated (Table 4). It is evident that the CeO_2/ZnO–0.4 sample offers the best performance, in terms of both conversion and mass-normalized specific activity, revealing its superior reactivity. It should be noted, however, that in terms of area-normalized activity, both bare ceria and mixed oxides exhibited an inferior activity as compared to bare ZnO. The latter can be attributed to the low surface area of ZnO (7.05 m^2/g), which is about one order of magnitude lower compared to bare CeO_2 and CeO_2/ZnO mixed oxides. Therefore, on the basis of the present results, the enhanced catalytic performance of CeO_2/ZnO mixed oxides can be attributed to a compromise between redox and surface

properties. Moreover, the optimum CeO_2/ZnO–0.4 sample exhibits an apparent activation energy (E_a) of 32.1 kJ/mol, much lower than that of bare ceria (44.2 kJ/mol), ZnO (42.1 kJ/mol) and CeO_2+ZnO–0.4 mechanical mixture (43.2 kJ/mol). These findings unveil the lower energy barrier for CO oxidation over the hydrothermally prepared mixed oxides, as compared to single oxides and mechanical mixture, demonstrating the beneficial synergistic interactions induced by synthesis procedure.

Table 4. Conversion of CO and specific rates of CeO_2 and CeO_2/ZnO samples at 200 °C. Reaction conditions: 0.2 vol.% CO and 1 vol.% O_2 in He.

Sample	CO Conversion (%)	Specific Rate	
		r ($\mu mol\ g^{-1}\ s^{-1}$)	r (×100) ($\mu mol\ m^{-2}\ s^{-1}$)
CeO_2	5.1	0.056	0.070
CeO_2/ZnO–0.2	5.4	0.059	0.077
CeO_2/ZnO–0.4	6.9	0.075	0.121
CeO_2/ZnO–0.6	6.2	0.068	0.121
ZnO	1.3	0.014	0.201

The CO oxidation process investigated here can be corroborated on the basis of a redox-type (Mars-van Krevelen) mechanism. This particular mechanism involves CO chemisorption on $Ce^{\delta+}$ active sites, followed by oxygen activation on oxygen vacancies [3,21,41]. CO oxidation is taking place between the $Ce^{\delta+}$–CO and adjacent oxygen species, followed by the regeneration of active sites and the reoccupation of oxygen vacancies through gas phase oxygen. The proposed reaction sequence is described in detail in our previous work [21].

In view of the above mechanistic aspects, the key role of the catalyst's redox properties is clearly manifested. In detail, the high oxygen storage capacity (Table 3), linked to enhanced reducibility and oxygen exchange kinetics, can be accounted for the improved oxidation performance. Any structural or compositional modification in ceria that can affect the ceria-oxygen or ceria-oxygen-metal bond can eventually facilitate O_2 activation and in turn CO oxidation. In this regard, we recently showed that the enhanced reducibility of CeO_2 nanorods, linked to their abundance in oxygen vacancies, is the pivotal factor for their superior catalytic performance [21]. Furthermore, we demonstrated that when a transition metal element is incorporated in the structure of ceria nanorods, even if catalytically non-active (i.e., Ti), it can affect oxygen species coordination environment and in turn the OSC and the catalytic performance [35].

These arguments in relation to the crucial role of reducibility are clearly supported by the direct relationship between the redox properties (OSC, mmol g^{-1}) and the normalized reaction rate ($\mu mol\ g^{-1}\ s^{-1}$), as shown in Figure 7. Interestingly, the key role of OSC as an activity descriptor is further demonstrated in the present work by including in Figure 7 relevant literature data, previously obtained with bare CeO_2 and CeO_2/TiO_2 oxides [2,35]. The latter is of particular importance towards the development of cost-effective and highly active metal oxides by appropriately adjusting their redox features.

Thus, regarding the present findings, although bare ZnO is catalytically far less active compared to CeO_2 (Figure 6), their combination results in a synergistic effect towards the formation of CeO_2/ZnO mixed oxides of improved activity. Similar synergistic interactions were previously revealed over TiO_2–doped CeO_2 [35], where, however, the doping element was incorporated in the nanostructure, resulting in the formation of Ce–O–Ti active sites. Notably, in the present work, ZnO is not incorporated in the CeO_2 nanorod structure. As clearly shown by TEM images (Figure 3), ZnO nanoparticles are in close interaction with nanorods but clearly as separate particles. This is also verified by the XRD results (Figure 2), which indicate distinct oxide phases without the formation of solid solution. Hence, the improved catalytic activity of CeO_2/ZnO mixed oxides, which is related to the population of active oxygen species and to the facile reduction of surface oxygen, can be attributed to the facilitation

of ceria capping oxygen reduction by adjacent ZnO nanoparticles, which in turn leads to higher OSC (Figure 5, Table 3). Thus, although ZnO is not incorporated in the ceria nanorods structure, it notably contributes to surface oxygen reduction, most likely through the interfacial ZnO–CeO_2 sites. The latter in combination with the abundance and lower cost of zinc compared to cerium oxide is a very interesting aspect in terms of catalyst design.
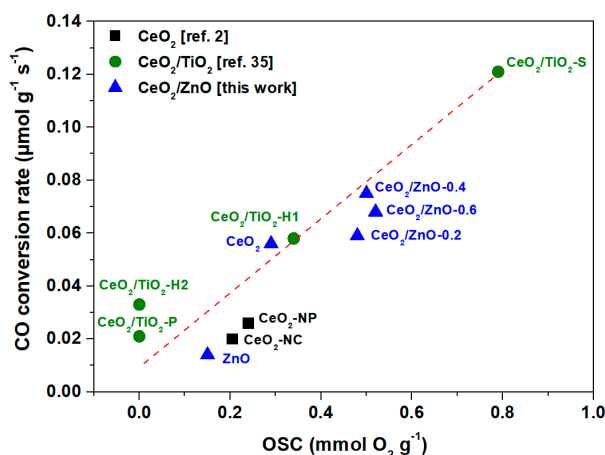

Figure 7. Correlation of specific activity with oxygen storage capacity (OSC). Literature data are also included. Specific rates were obtained at 200 °C under the reaction conditions: 0.2 vol.% CO and 1 vol.% O_2 in He. The dotted line simply represents the general trend of the data. The designation of the samples inside the figure refers to CeO_2 nanopolyhedra (CeO_2–NP), CeO_2 nanocubes (CeO_2–NC), CeO_2–TiO_2 nanoparticles prepared by precipitation (CeO_2/TiO_2–P), hydrothermal method in one and two steps (CeO_2/TiO_2–H1 and CeO_2/TiO_2–H2, respectively) and Stöber method (CeO_2/TiO_2–S).

4. Conclusions

In the present work, CeO_2/ZnO mixed oxides were synthesized by a two-step hydrothermal method. A thorough characterization study was carried out, revealing their textural, structural, morphological and redox features. CO oxidation was employed as a probe reaction to gain insight into the structure-activity relationships. The following order, both in terms of CO conversion and specific activity, was obtained: CeO_2/ZnO–0.4 > CeO_2/ZnO–0.6 > CeO_2/ZnO–0.2 > CeO_2 > ZnO. Despite the distinct appearance of ZnO and CeO_2 phases in mixed oxides and the low reactivity of ZnO, mixed oxides exhibit improved catalytic performance as compared to bare ones. The latter was attributed to the synergistic CeO_2–ZnO interactions towards an improved oxygen mobility and reducibility. Interestingly, a close relationship between the catalytic activity and the oxygen storage capacity was disclosed. Moreover, comparison with relevant literature studies verifies the role of OSC as a key activity descriptor for reactions following a redox-type mechanism. The present work reveals the significance of the rational design of noble metal-free mixed oxides towards the development of highly active materials that can be used in a variety of environmental and energy-related processes.

Author Contributions: S.S., M.L., V.B. and P.K.P. contributed to materials synthesis and characterization, results interpretation and paper–writing; V.N.S. and M.K. contributed to the conception, design, results interpretation and writing of the paper. M.K. reviewed, edited and submitted the manuscript in the final form. All authors have read and agreed to the published version of the manuscript.

Conflicts of Interest: The authors declare no conflict of interest.

References

1. Lykaki, M.; Pachatouridou, E.; Iliopoulou, E.; Carabineiro, S.A.C.; Konsolakis, M. Impact of the synthesis parameters on the solid state properties and the CO oxidation performance of ceria nanoparticles. *RSC Adv.* **2017**, *7*, 6160–6169. [CrossRef]

2. Lykaki, M.; Stefa, S.; Carabineiro, S.A.C.; Pandis, P.K.; Stathopoulos, V.N.; Konsolakis, M. Facet-Dependent Reactivity of Fe_2O_3/CeO_2 Nanocomposites: Effect of Ceria Morphology on CO Oxidation. *Catalysts* **2019**, *9*, 371. [CrossRef]

3. Wu, Z.; Li, M.; Overbury, S.H. On the structure dependence of CO oxidation over CeO_2 nanocrystals with well-defined surface planes. *J. Catal.* **2012**, *285*, 61–73. [CrossRef]

4. Zhang, S.; Li, Y.; Huang, J.; Lee, J.; Kim, D.H.; Frenkel, A.I.; Kim, T. Effects of Molecular and Electronic Structures in CoO_x/CeO_2 Catalysts on NO Reduction by CO. *J. Phys. Chem. C* **2019**, *123*, 7166–7177. [CrossRef]

5. Zhang, S.; Lee, J.; Kim, D.H.; Kim, T. NO reduction by CO over CoO_x/CeO_2 catalysts: Effect of support calcination temperature on activity. *Mol. Catal.* **2020**, *482*, 110703. [CrossRef]

6. Akter, N.; Zhang, S.; Lee, J.; Kim, D.H.; Boscoboinik, J.A.; Kim, T. Selective catalytic reduction of NO by ammonia and NO oxidation Over CoO_x/CeO_2 catalysts. *Mol. Catal.* **2020**, *482*, 110664. [CrossRef]

7. Cámara, A.L.; Corberán, V.C.; Martínez-Arias, A.; Barrio, L.; Si, R.; Hanson, J.C.; Rodriguez, J.A. Novel manganese-promoted inverse CeO_2/CuO catalyst: In situ characterization and activity for the water-gas shift reaction. *Catal. Today* **2020**, *339*, 24–31. [CrossRef]

8. Chen, C.; Zhan, Y.; Zhou, J.; Li, D.; Zhang, Y.; Lin, X.; Jiang, L.; Zheng, Q. Cu/CeO_2 Catalyst for Water-Gas Shift Reaction: Effect of CeO_2 Pretreatment. *ChemPhysChem* **2018**, *19*, 1448–1455. [CrossRef] [PubMed]

9. Ronda-Lloret, M.; Rico-Francés, S.; Sepúlveda-Escribano, A.; Ramos-Fernandez, E.V. CuO_x/CeO_2 catalyst derived from metal organic framework for reverse water-gas shift reaction. *Appl. Catal. A Gen.* **2018**, *562*, 28–36. [CrossRef]

10. Damaskinos, C.M.; Vasiliades, M.A.; Stathopoulos, V.N.; Efstathiou, A.M. The Effect of CeO_2 Preparation Method on the Carbon Pathways in the Dry Reforming of Methane on Ni/CeO_2 Studied by Transient Techniques. *Catalysts* **2019**, *9*, 621. [CrossRef]

11. Da Silva, A.M.; De Souza, K.R.; Jacobs, G.; Graham, U.M.; Davis, B.H.; Mattos, L.V.; Noronha, F.B. Steam and CO_2 reforming of ethanol over Rh/CeO_2 catalyst. *Appl. Catal. B Environ.* **2011**, *102*, 94–109. [CrossRef]

12. Hou, T.; Yu, B.; Zhang, S.; Xu, T.; Wang, D.; Cai, W. Hydrogen production from ethanol steam reforming over Rh/CeO_2 catalyst. *Catal. Commun.* **2015**, *58*, 137–140. [CrossRef]

13. Kumar, P.A.; Tanwar, M.D.; Russo, N.; Pirone, R.; Fino, D. Synthesis and catalytic properties of CeO_2 and Co/CeO_2 nanofibres for diesel soot combustion. *Catal. Today* **2012**, *184*, 279–287. [CrossRef]

14. Muroyama, H.; Hano, S.; Matsui, T.; Eguchi, K. Catalytic soot combustion over CeO_2-based oxides. *Catal. Today* **2010**, *153*, 133–135. [CrossRef]

15. Aneggi, E.; Wiater, D.; de Leitenburg, C.; Llorca, J.; Trovarelli, A. Shape-Dependent Activity of Ceria in Soot Combustion. *ACS Catal.* **2014**, *4*, 172–181. [CrossRef]

16. Konsolakis, M.; Lykaki, M. Recent Advances on the Rational Design of Non-Precious Metal Oxide Catalysts Exemplified by CuO_x/CeO_2 Binary System: Implications of Size, Shape and Electronic Effects on Intrinsic Reactivity and Metal-Support Interactions. *Catalysts* **2020**, *10*, 160. [CrossRef]

17. Montini, T.; Melchionna, M.; Monai, M.; Fornasiero, P. Fundamentals and Catalytic Applications of CeO_2-Based Materials. *Chem. Rev.* **2016**, *116*, 5987–6041. [CrossRef]

18. Paier, J.; Penschke, C.; Sauer, J. Oxygen Defects and Surface Chemistry of Ceria: Quantum Chemical Studies Compared to Experiment. *Chem. Rev.* **2013**, *113*, 3949–3985. [CrossRef]

19. Cargnello, M.; Doan-Nguyen, V.V.T.; Gordon, T.R.; Diaz, R.E.; Stach, E.A.; Gorte, R.J.; Fornasiero, P.; Murray, C.B. Control of Metal Nanocrystal Size Reveals Metal-Support Interface Role for Ceria Catalysts. *Science* **2013**, *341*, 771–773. [CrossRef]

20. Tang, W.-X.; Gao, P.-X. Nanostructured cerium oxide: Preparation, characterization, and application in energy and environmental catalysis. *MRS Commun.* **2016**, *6*, 311–329. [CrossRef]

21. Lykaki, M.; Pachatouridou, E.; Carabineiro, S.A.C.; Iliopoulou, E.; Andriopoulou, C.; Kallithrakas-Kontos, N.; Boghosian, S.; Konsolakis, M. Ceria nanoparticles shape effects on the structural defects and surface chemistry: Implications in CO oxidation by Cu/CeO_2 catalysts. *Appl. Catal. B Environ.* **2018**, *230*, 18–28. [CrossRef]

22. Elias, J.S.; Risch, M.; Giordano, L.; Mansour, A.N.; Shao-Horn, Y. Structure, Bonding, and Catalytic Activity of Monodisperse, Transition-Metal-Substituted CeO_2 Nanoparticles. *J. Am. Chem. Soc.* **2014**, *136*, 17193–17200. [CrossRef] [PubMed]

23. Bion, N.; Epron, F.; Moreno, M.; Mariño, F.; Duprez, D. Preferential Oxidation of Carbon Monoxide in the Presence of Hydrogen (PROX) over Noble Metals and Transition Metal Oxides: Advantages and Drawbacks. *Top. Catal.* **2008**, *51*, 76–88. [CrossRef]

24. Wang, J.; Chen, R.; Xiang, L.; Komarneni, S. Synthesis, properties and applications of ZnO nanomaterials with oxygen vacancies: A review. *Ceram. Int.* **2018**, *44*, 7357–7377. [CrossRef]

25. Sajjad, M.; Ullah, I.; Khan, M.I.; Khan, J.; Khan, M.Y.; Qureshi, M.T. Structural and optical properties of pure and copper doped zinc oxide nanoparticles. *Results Phys.* **2018**, *9*, 1301–1309. [CrossRef]

26. Lee, C.-G.; Na, K.-H.; Kim, W.-T.; Park, D.-C.; Yang, W.-H.; Choi, W.-Y. TiO_2/ZnO Nanofibers Prepared by Electrospinning and Their Photocatalytic Degradation of Methylene Blue Compared with TiO_2 Nanofibers. *Appl. Sci.* **2019**, *9*, 3404. [CrossRef]

27. Stathopoulos, V.N.; Papandreou, A.; Kanellopoulou, D.; Stournaras, C.J. Structural ceramics containing electric arc furnace dust. *J. Hazard. Mater.* **2013**, *262*, 91–99. [CrossRef]

28. Rodwihok, C.; Wongratanaphisan, D.; Van Tam, T.; Choi, W.M.; Hur, S.H.; Chung, J.S. Cerium-Oxide-Nanoparticle-Decorated Zinc Oxide with Enhanced Photocatalytic Degradation of Methyl Orange. *Appl. Sci.* **2020**, *10*, 1697. [CrossRef]

29. Ma, T.-Y.; Yuan, Z.-Y.; Cao, J.-L. Hydrangea-Like Meso-/Macroporous ZnO-CeO_2 Binary Oxide Materials: Synthesis, Photocatalysis and CO Oxidation. *Eur. J. Inorg. Chem.* **2010**, *2010*, 716–724. [CrossRef]

30. Lv, Z.; Zhong, Q.; Ou, M. Utilizing peroxide as precursor for the synthesis of CeO_2/ZnO composite oxide with enhanced photocatalytic activity. *Appl. Surf. Sci.* **2016**, *376*, 91–96. [CrossRef]

31. De Lima, J.F.; Martins, R.F.; Neri, C.R.; Serra, O.A. ZnO:CeO_2-based nanopowders with low catalytic activity as UV absorbers. *Appl. Surf. Sci.* **2009**, *255*, 9006–9009. [CrossRef]

32. Liu, I.-T.; Hon, M.-H.; Teoh, L.G. The preparation, characterization and photocatalytic activity of radical-shaped CeO_2/ZnO microstructures. *Ceram. Int.* **2014**, *40*, 4019–4024. [CrossRef]

33. Xie, Q.; Zhao, Y.; Guo, H.; Lu, A.; Zhang, X.; Wang, L.; Chen, M.-S.; Peng, D.-L. Facile Preparation of Well-Dispersed CeO_2–ZnO Composite Hollow Microspheres with Enhanced Catalytic Activity for CO Oxidation. *ACS Appl. Mater. Interfaces* **2014**, *6*, 421–428. [CrossRef] [PubMed]

34. Mu, G.; Liu, C.; Wei, Q.; Huang, Y. Three dimensionally ordered macroporous CeO_2-ZnO catalysts for enhanced CO oxidation. *Mater. Lett.* **2016**, *181*, 161–164. [CrossRef]

35. Stefa, S.; Lykaki, M.; Fragkoulis, D.; Binas, V.; Pandis, P.K.; Stathopoulos, V.N.; Konsolakis, M. Effect of the Preparation Method on the Physicochemical Properties and the CO Oxidation Performance of Nanostructured CeO_2/TiO_2 Oxides. *Processes* **2020**, *8*, 847. [CrossRef]

36. Luo, J.-Y.; Meng, M.; Li, X.; Li, X.-G.; Zha, Y.-Q.; Hu, T.-D.; Xie, Y.-N.; Zhang, J. Mesoporous Co_3O_4–CeO_2 and Pd/Co_3O_4–CeO_2 catalysts: Synthesis, characterization and mechanistic study of their catalytic properties for low-temperature CO oxidation. *J. Catal.* **2008**, *254*, 310–324. [CrossRef]

37. Liu, J.; Zhao, Z.; Wang, J.; Xu, C.; Duan, A.; Jiang, G.; Yang, Q. The highly active catalysts of nanometric CeO_2-supported cobalt oxides for soot combustion. *Appl. Catal. B Environ.* **2008**, *84*, 185–195. [CrossRef]

38. Yu, S.-W.; Huang, H.-H.; Tang, C.-W.; Wang, C.-B. The effect of accessible oxygen over Co_3O_4–CeO_2 catalysts on the steam reforming of ethanol. *Int. J. Hydrogen Energy* **2014**, *39*, 20700–20711. [CrossRef]

39. Subramanian, V.; Potdar, H.S.; Jeong, D.-W.; Shim, J.-O.; Jang, W.-J.; Roh, H.-S.; Jung, U.H.; Yoon, W.L. Synthesis of a Novel Nano-Sized Pt/ZnO Catalyst for Water Gas Shift Reaction in Medium Temperature Application. *Catal. Lett.* **2012**, *142*, 1075–1081. [CrossRef]

40. Khan, A.; Smirniotis, P.G. Relationship between temperature-programmed reduction profile and activity of modified ferrite-based catalysts for WGS reaction. *J. Mol. Catal. A Chem.* **2008**, *280*, 43–51. [CrossRef]

41. Mukherjee, D.; Rao, B.G.; Reddy, B.M. CO and soot oxidation activity of doped ceria: Influence of dopants. *Appl. Catal. B Environ.* **2016**, *197*, 105–115. [CrossRef]